Research Article | Vol. 24, No. 19 | 19 Sep 2016 | OPTICS EXPRESS 21921

Optics EXPRESS

Laser induced ultrasonic phased array using full matrix capture data acquisition and total focusing method

THEODOSIA STRATOUDAKI,[1,2,*] MATT CLARK,[2] AND PAUL D. WILCOX[1]

[1]*Department of Mechanical Engineering, University of Bristol, University Walk, Bristol, BS8 1TR, UK*
[2]*Division of Electrical Systems and Optics, Faculty of Engineering, University of Nottingham, University Park, Nottingham, NG7 2RD, UK*
[*]*t.stratoudaki@physics.org*

Abstract: Laser ultrasonics is a technique where lasers are employed to generate and detect ultrasound. A data collection method (full matrix capture) and a post processing imaging algorithm, the total focusing method, both developed for ultrasonic arrays, are modified and used in order to enhance the capabilities of laser ultrasonics for nondestructive testing by improving defect detectability and increasing spatial resolution. In this way, a laser induced ultrasonic phased array is synthesized. A model is developed and compared with experimental results from aluminum samples with side drilled holes and slots at depths of 5 - 20 mm from the surface.

OCIS codes: (280.3375) Laser induced ultrasonics; (110.5100) Phased-array imaging systems; (120.0280) Remote sensing and sensors; (120.4290) Nondestructive testing; (110.7170) Ultrasound.

References and links

1. S. J. Davies, C. Edwards, G. S. Taylor, and S. B. Palmer, "Laser generated ultrasound: its properties, mechanisms and multifarious applications," J. Phys. D Appl. Phys. **26**, 329–348 (1993).
2. C. B. Scruby and L. E. Drain, *Laser Ultrasonics, Techniques and Applications* (Adam Hilger, 1990).
3. P. A. Doyle, "On optical waveform for laser-generated ultrasound," J. Phys. D Appl. Phys. **19**, 1613–1623 (1986).
4. K. L. Telschow and R. J. Conant, "Optical and thermal parameter effects on laser-generated ultrasound," J. Acoust. Soc. Am. **88**, 1494–1502 (1990).
5. L. R. F. Rose, "Point-source representation for laser-generated ultrasound," J. Acoust. Soc. Am. **75**, 723–732 (1984).
6. J. P. Monchalin, "Optical detection of ultrasound," IEEE T. Ultrason. Ferr. **33**, 485–499 (1986).
7. L. S. Wang, J. S. Steckenrider, and J. D. Achenbach, "A fiber-based laser ultrasonic system for remote inspection of limited access components," in *Review of Progress in Quantitative Nondestructive Evaluation*, vol. 16 (Plenum, 1997), pp. 507–514.
8. M. Dubois, M. Militzer, A. Moreau, and J. F. Bussiere, "A new technique for the quantitative real-time monitoring of austenite grain growth in steel," Scripta Mater. **42**, 867–874 (2000).
9. K. R. Yawn, M. A. Osterkamp, D. Kaiser, and C. Barina, "Improved laser ultrasonic systems for industry," in *Review of Progress in Quantitative Nondestructive Evaluation*, vol. 1581 (AIP, 2014), pp. 397–404.
10. R. E. Lee and R. M. White, "Excitation of surface elastic waves by transient surface heating," Appl. Phys. Lett. **12**, 12–14 (1968).
11. M. Clark, S. D. Sharples, and M. G. Somekh, "Diffractive acoustic elements for laser ultrasonics," J. Acoust. Soc. Am. **107**, 3179–3185 (2000).
12. S. D. Sharples, M. Clark, and M. G. Somekh, "All-optical adaptive scanning acoustic microscope," Ultrasonics **41**, 295–299 (2003).
13. T. Stratoudaki, M. Clark, and M. G. Somekh, "Cheap optical transducers (CHOTS) for generation and detection of longitudinal waves," in *2012 IEEE International Ultrasonics Symposium* (IEEE, 2012), pp. 961–964.
14. A. J. A. Bruinsma and J. A. Vogel, "Ultrasonic noncontact inspection system with optical fiber," Appl. Optics **27**, 4690–4695 (1988).
15. J. Jarzynski and Y. H. Berthelot, "The use of optical fibers to enhance the laser generation of ultrasonic waves," J. Acoust. Soc. Am. **8**, 158–162 (1989).
16. S. N. Hopko, I. C. Ume, and D. S. Erdahl, "Development of a flexible laser ultrasonic probe," J. Manuf. Sci. E. - T. ASME **124**, 351–357 (2002).
17. B. Mi and C. Ume, "Real-time weld penetration depth monitoring with laser ultrasonic sensing system," J. Manuf. Sci. E. - T. ASME **128**, 280–286 (2006).

#268686 http://dx.doi.org/10.1364/OE.24.021921
Journal © 2016 Received 17 Jun 2016; revised 21 Jul 2016; accepted 9 Aug 2016; published 12 Sep 2016

Optics EXPRESS

18. C. Pei, K. Demachi, T. Fukuchi, K. Koyama, and M. Uesaka, "Cracks measurement using fiber-phased array laser ultrasound generation," J. Appl. Phys. **113**, 163101 (2013).
19. J. S. Steckenrider, T. W. Murray, J. B. D. Jr., and J. W. Wagner, "Sensitivity enhancement in laser ultrasonics using a versatile laser array system," J. Acoust. Soc. Am. **97**, 273–279 (1995).
20. J. T. W. Murray, J. B. Deaton and J. W. Wagner, "Experimental evaluation of enhanced generation of ultrasonic waves using an array of laser sources," Ultrasonics **34**, 69–77 (1996).
21. M.-H. Noroy, D. Royer, and M. Fink, "The laser-generated ultrasonic phased array: Analysis and experiments," J. Acoust. Soc. Am. **94**, 1934–1943 (1993).
22. M.-H. Noroy, D. Royer, and M. Fink, "Shear-wave focusing with a laser-ultrasound phased-array," IEEE T. Ultrason. Ferr. **42**, 981–988 (1995).
23. A. Blouin, D. Levesque, C. Neron, D. Drolet, and J.-P. Monchalin, "Improved resolution and signal-to-noise ratio in laser-ultrasonics by saft processing," Opt. Express **2**, 531–539 (1998).
24. D. Levesque, A. Blouin, C. Neron, and J.-P. Monchalin, "Performance of laser-ultrasonic F-SAFT imaging," Ultrasonics **40**, 1057âĂŞ1063 (2002).
25. P. D. W. C. Holmes, B. W. Drinkwater, "Post-processing of the full matrix of ultrasonic transmitâĂŞreceive array data for non-destructive evaluation," NDT&E Int. **38**, 701âĂŞ711 (2005).
26. P. D. W. C. Holmes, B. W. Drinkwater, "Advanced post-processing for scanned ultrasonic arrays: Application to defect detection and classification in non-destructive evaluation," Ultrasonics **48**, 636âĂŞ642 (2008).
27. R. M. White, "Generation of elastic waves by transient surface heating," J. Appl. Phys. **34**, 3559–3567 (1963).
28. J. R. Bernstein and J. B. Spicer, "Line source representation for laser-generated ultrasound in aluminum," J. Acoust. Soc. Am. **107**, 1352–1357 (2000).
29. G. F. Miller and H. Pursey, "The field and radiation impedance of mechanical radiators on the free surface of a semi-infinite isotropic solid," in *Proceedings of the Royal Society of London. Series A, Mathematical and Physical Sciences*, vol. 223 (Royal Society, 1954), pp. 521–542.
30. J. Zhang, B. W. Drinkwater, and P. D. Wilcox, "Defect characterization using an ultrasonic array to measure the scattering coefĩňĄcient matrix," IEEE T. Ultrason. Ferr. **55**, 2254–2265 (2008).
31. A. L. Lopez-Sanchez, H. J. Kim, L. W. Schmerr, and A. Sedov, "Measurement models and scattering models for predicting the ultrasonic pulse-echo response from side-drilled holes," J. Nondestruct. Eval. **24**, 83–96 (2005).
32. E. Glushkov, N. Glushkova, A. Ekhlakov, and E. Shapar, "An analytically based computer model for surface measurements in ultrasonic crack detection," Wave Motion **43**, 458–473 (2006).
33. C. Li, D. Pain, P. D. Wilcox, and B. W. Drinkwater, "Imaging composite material using ultrasonic arrays," NDT&E Int. **53**, 8–17 (2013).
34. S. Raetz, T. Dehoux, and B. Audoin, "Effect of laser beam incidence angle on the thermoelastic generation in semi-transparent materials," J. Acoust. Soc. Am. **130**, 3691âĂŞ3697 (2011).
35. E. Palik, *Handbook of Optical Constants of Solids* (Academic, 1998).
36. S. C. Wooh and Y. Shi, "Optimum beam steering of linear phased arrays," Wave Motion **29**, 245–265 (1999).
37. G. Rousseau and A. Blouin, "Hadamard multiplexing in laser ultrasonics," Opt. Express **20**, 25798–25816 (2012).
38. J. Davies, F. Simonetti, M. Lowe, and P. Cawley, "Review of synthetically focused guided wave imaging techniques with application to defect sizing," in *Review of Progress in Quantitative Nondestructive Evaluation*, vol. 25 (Plenum, 2006), pp. 142–149.
39. P. D. Wilcox, "Ultrasonic arrays in nde: Beyond the b-scan," in *Review of Progress in Quantitative Nondestructive Evaluation*, vol. 1151 (AIP, 2013), pp. 33–50.
40. Y.-J. Chen, "Relationship between ultrasonic characteristics and relative porosity in Al and Al-XSi alloys," Mater. Trans. **50**, 2308–2313 (2009).
41. J. Wagner and J. Spicer, "Theoretical noise-limited sensitivity of classical interferometry," J. Opt. Soc. Am. **4**, 1316–1326 (1987).
42. A. M. Aindow, R. J. Dewhurst, D. A. Hutchins, and S. B. Palmer, "Laser-generated ultrasonic pulses at free metal surfaces," J. Acoust. Soc. Am. **69**, 449–455 (1981).
43. J. Wagner, "Breaking the sensitivity barrier: the challenge for laser ultrasonics," in *Proceedings of IEEE Ultrasonics Symposium*, vol. 1 and 2 (IEEE, 1992), pp. 791–800.
44. J. P. Monchalin, "Progress towards the application of laser-ultrasonics in industry," in *Review of Progress in Quantitative Nondestructive Evaluation*, vol. 11 (Plenum, 1993), pp. 495–506.
45. J. P. Monchalin and R. Heon, "Broadband optical detection of ultrasound by sideband stripping with a confocal Fabry-Pérot," Appl. Phys. Lett. **55**, 1612–1614 (1989).
46. P. Delaye, A. Blouin, D. Drolet, L. A. deMontmorillon, G. Roosen, and J. P. Monchalin, "Detection of ultrasonic motion of a scattering surface by photorefractive inp:fe under an applied dc field," J. Opt. Soc. Am. **14**, 1723–1734 (1997).
47. P. V. Mitchell, G. J. Dunning, S. W. McCahon, M. B. Klein, T. R. OâĂŹMeara, and D. M. Pepper, "Compensated high-bandwidth laser ultrasonic detector based on photo-induced emf in GaAs," in *Review of Progress in Quantitative Nondestructive Evaluation*, vol. 15 (Plenum, 1996), pp. 2149–2155.
48. T. W. Murray and S. Krishnaswamy, "Multiplexed interferometer for ultrasonic imaging applications," Opt. Eng. **40**, 1321–1328 (2001).
49. A. I. Bowler, B. W. Drinkwater, and P. D. Wilcox, "An investigation into the feasibility of internal strain measurement

Optics EXPRESS

in solids by correlation of ultrasonic images," P. Roy. Soc. A-Math. Phy. **467**, 2247–2270 (2011).

1. Introduction

Laser ultrasonics is a technique where lasers are used for the generation and detection of ultrasound instead of conventional piezoelectric transducers [1, 2]. The light of a pulsed laser is focused onto the surface of the component to be tested and is absorbed. In metals, the absorption of light happens predominantly within the electromagnetic skin depth, which is a few nanometers. The absorbed light heats up the irradiated component and thermal diffusion further extends the region of local heating to a depth of around one micron [3, 4]. The heating causes rapid expansion at times that are comparable to the rise time of the laser pulse (nanoseconds duration) [5]. This fast, thermo-elastic expansion is the source of the generated ultrasonic wave. The wave then travels through the component and is detected optically, usually by some type of laser interferometer [6]. Laser ultrasonics has several advantages over conventional ultrasonic methods: it is a non contact and couplant free technique, making it suitable for places with limited access [7], hazardous environments [8] and inspection of geometrically complex components [9]. It is also a broadband technique and all modes of ultrasonic waves (e.g. longitudinal, shear, surface waves) are excited.

The use of ultrasonic phased arrays has had a major impact on science, medicine and society, since their first appearance in the late âĂŸ60s. During the last decade, there has been a rapid increase in the use of ultrasonic arrays for nondestructive testing (NDT) applications. A conventional ultrasonic array is made of several ultrasonic transducer elements which can be addressed individually to transmit and receive ultrasonic signals. A phased array can control the directivity and focus of the ultrasound by varying the time delay between the firings of the array elements. The benefits of phased arrays are increased image quality and flexibility regarding the range of different inspections (e.g. plane, focused, steered ultrasonic beams can be injected into a sample) that can be done from a single location of the array.

Laser induced ultrasonic arrays have been proposed as early as 1968 [10] by spatial modification of the laser beam. Using this method, previous work from the authors of the present article, has shown successful control of focusing and steering of surface acoustic waves and longitudinal waves [11–13]. Another option is to use temporal modification of the laser and two methods of phased arrays using laser ultrasonics have been proposed in the past: using a single laser source with multiple optical delays and using multiple laser sources. The first method uses a single laser source which is then split and delivered to the target following a range of optical delay paths to achieve the desired time delay. This can be achieved by using multiple optical fibers of variable length [14–18], or a White cell optical delay cavity system [19]. The second method uses an array of laser cavities, fired at the desired time delay [20–22]. Both these methods are expensive in terms of hardware. The main disadvantage of using optical fibers for delivery of high-energy laser pulses is that the amount of energy delivered must be limited to a level that the fiber can withstand, while using either fibers or a White cell optical delay cavity requires complicated optical setups. The main disadvantage of using multiple laser sources is the cost of the system, and a second disadvantage is the portability of such a system.

An alternative philosophy to array imaging is to perform the imaging in post processing. Previous authors have used the synthetic aperture focusing technique (SAFT) with laser ultrasonics to improve detectability and enhance images [23, 24], mainly in the destructive, ablative regime. The first aim of the present paper is to demonstrate Laser Induced Phased Array (LIPA) imaging in post processing, by obtaining the full matrix of all possible transmitter receiver combinations in the array, at the nondestructive, thermoelastic regime. This data acquisition method is known as Full Matrix Capture (FMC) [25, 26]. A major benefit of this method is that now a whole range of imaging algorithms can be applied to the same data set, in post processing. For laser ultrasonics

Optics EXPRESS

in particular, the advantage is that array configurations can now be synthesized without the need of complicated optical setups and without being limited by the physical constraints (e.g. restrictions on the number of array elements) that come with these setups. The second aim of the paper is to present results of nondestructive testing using the Total Focusing Method (TFM) [25] as the imaging algorithm. Results are also presented using SAFT and the two algorithms are compared.

Section 2 presents the background of the laser ultrasonic generation and detection mechanism in the nondestructive, thermoelastic regime, as well as the theory of the FMC and the TFM algorithm, adapted for LIPAs. Section 3 presents the experimental setup and experimental results from aluminum samples with side drilled holes and slots at depths ranging from 5 to 20 mm from the surface. Section 4 presents a discussion of the technique and its limitations and explains how, in principle, some of the current limitations could be overcome. Finally, Section 5 presents the conclusions.

2. Principles of laser ultrasonic generation and detection using an array of sources

Ultrasound is generated when the light emitted by a pulsed laser is absorbed by the material. In the low laser power, thermoelastic regime, there is no damage of the material and the process is nondestructive [27]. The laser beam incident to the sample, locally heats its surface and causes it to expand rapidly, at times that are comparable to the pulse length of the laser, which -for the cases considered in the work presented here- is of the order of 1 ns. As the laser energy is absorbed in a layer much thinner than the ultrasonic wavelength (a few nanometers in aluminum), the bandwidth of the generated wave depends on the temporal characteristics of the laser pulse and is broadband [2]; longitudinal, shear and surface acoustic waves can be generated. A point source has been used for most practical applications [3, 5]. In certain cases, it is advantageous to use a laser line source rather than a point; for example, a line source spreads the generating light over a larger area, reducing the peak intensity as well as enhancing the wave directivity. A line source has been used in the experiments presented here and in this case, the angular dependence of the amplitude of the longitudinal and the shear waves are given respectively by [22, 28]:

$$G_L(\theta) \propto \frac{\sin\theta \sin 2\theta(\kappa^2 - \sin^2\theta)^{1/2}}{2\sin\theta \sin 2\theta(\kappa^2 - \sin^2\theta)^{1/2} + (\kappa^2 - 2\sin^2\theta)^2} \tag{1}$$

$$G_T(\theta) \propto \frac{\sin 2\theta \cos 2\theta}{\cos^2 2\theta + 2\sin\theta \sin 2\theta(\kappa^{-2} - \sin^2\theta)^{1/2}} \tag{2}$$

where θ is the observation angle with respect to the surface normal and $\kappa = c_L/c_T$, with c_L and c_T the acoustic velocities of the longitudinal and the shear wave respectively. In the case of aluminum, the directivity pattern of the longitudinal waves [21] has its maxima at $\theta = \pm 64^o$ and for shear waves [21, 28] the maxima are at $\theta = \pm 30^o$. A plot of the directivity of the longitudinal and shear waves, using Eq. (1) and Eq. (2) is shown in Figs. 1(a) and 1(b). In the nondestructive, thermoelastic regime, which was of interest to this study, shear waves are more efficiently produced than longitudinal waves [5]. It has been shown [5], that for aluminum, at this regime, the ratio of the radiated energy between longitudinal and shear waves is ~0.1, meaning that approx. 10 times more energy is radiated by the shear wave than the longitudinal. Consequently, the thermoelastically generated shear waves have greater amplitude than the longitudinal waves, although their directivity patterns, hence the angles at which they are observed, are different.

In this paper, an array of sources is made by scanning the generation beam; scanning the detection beam creates an array of detectors. The detector used in the work presented here, is sensitive to the out-of-plane ultrasonic component. The sensitivity of the detector to longitudinal

Optics EXPRESS

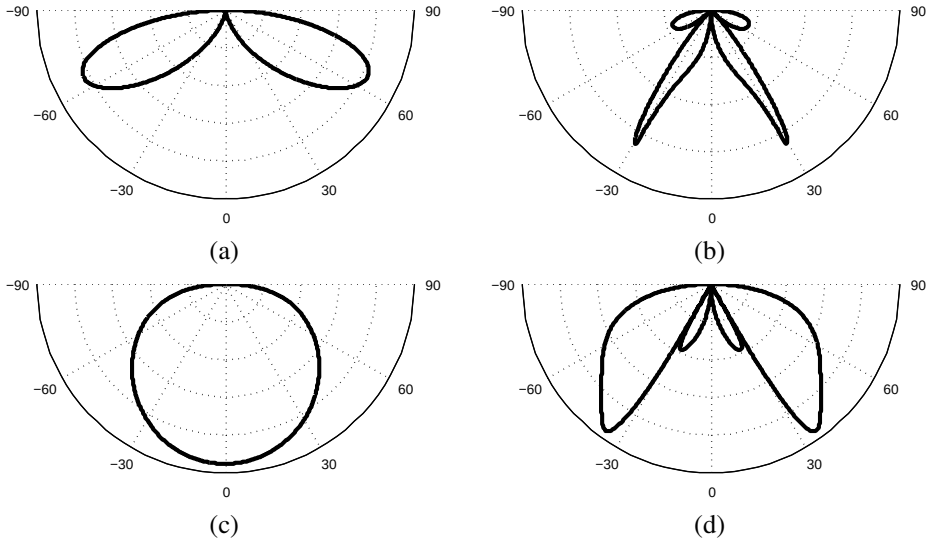

Fig. 1. (a) Directivity pattern of longitudinal (G_L) and (b) shear waves (G_T), in aluminum, in the thermoelastic regime. (c) Sensitivity of the detector to longitudinal (D_L) and (d) shear waves (D_T), in aluminum, as a function of wave angle.

and shear waves as a function of incident wave angle, is given, respectively, by [29]:

$$D_L(\theta) =\propto \frac{\cos\theta(\kappa^2 - 2\sin^2\theta)}{F_0(\sin\theta)} \tag{3}$$

$$D_T(\theta) \propto \frac{\sin 2\theta(\kappa^2 \sin^2\theta - 1)^{1/2}}{F_0(\kappa\sin\theta)} \tag{4}$$

$$\text{where } F_0(\xi) = (2\xi^2 - \kappa^2)^2 - 4\xi^2(\xi^2 - 1)^{1/2}(\xi^2 - \kappa^2)^{1/2} \tag{5}$$

Eq. (3) and Eq. (4) are actually the relations for the radial (compressional) and tangential (shear) components respectively, of an excited wave due to an out-of-plane point load on the surface. By reciprocity, these should be proportional to the out-of-plane surface displacement as a function of incident wave angle. A plot of Eq. (3) and Eq. (4) is shown in Figs. 1(c) and 1(d).

FMC is a data acquisition method developed for conventional ultrasonic arrays, where the waveform from every possible combination of transducer/receiver of an n element array is captured and forms a $n \times n$ matrix, the full matrix [25]. The experimental approach followed here in order to adapt the FMC to data from laser sources, is depicted in Fig. 2, as well as a representation of the full matrix. The beam of the generation laser is focused onto a line at the surface of the sample, along the y-axis and the beam of the detection laser is focused onto a spot. The laser beams are scanned in such a way along the x-axis (see Section 3.1) that the collected data correspond to those of a linear array with equi-spaced elements.

Because the generation and detection angular sensitivities are different, it is not readily apparent how this will affect the imaging performance of the system. For this reason, a forward model is desirable to predict the FMC data set, $h_{gd}(t)$ (where the indices g and d refer to ultrasonic generation and detection positions respectively). The model employed is a ray-based model that simulates the response of the system to one or more small targets. In the case of multiple targets, only first-order scattering is considered, hence the response of the system is simply the superposition of its response to each target, individually. Each target generates four

Optics EXPRESS

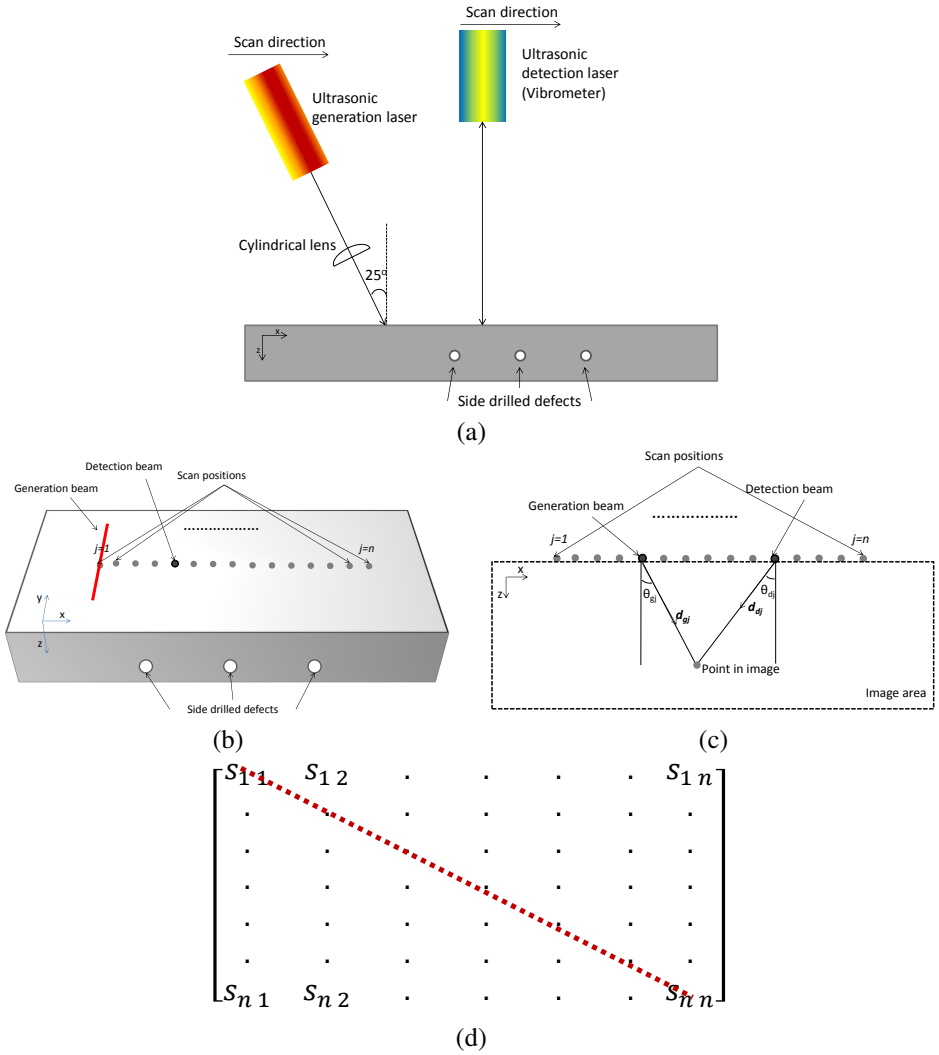

Fig. 2. Experimental setup, side view (a) and top view (b). The scan was parallel to the x-axis, on the xy-plane, and the defects were parallel to the y-axis. (c) Schematic diagram showing angles and path lengths. (d) The full matrix composed from all signals (s_{gd}). The red, dotted line indicates the set of data used with the SAFT algorithm.

Optics EXPRESS

separate responses corresponding to the four possible combinations of generated mode and detected mode (longitudinal-longitudinal, longitudinal-shear, shear-longitudinal and shear-shear). Again, these are treated separately and superposed. In the frequency, ω, domain, the response to the j^{th} target for generated mode, α =L or T (L for longitudinal and T for shear), and detected mode, β =L or T, can be written as:

$$H_{gdj}^{\alpha\beta}(\omega) = \frac{G_\alpha(\theta_{gj})D_\beta(\theta_{dj})}{(|\mathbf{d_{gj}}||\mathbf{d_{dj}}|)^{1/2}}\exp\left[-i\omega\left(\frac{|\mathbf{d_{gj}}|}{c_\alpha}+\frac{|\mathbf{d_{dj}}|}{c_\beta}\right)\right]A_j^{\alpha\beta}(\theta_{gj},\theta_{dj},\omega) \tag{6}$$

where θ_{gj} and θ_{dj} are the angles (relative to the surface normal) of the rays between the generation and detection positions and the target, $\mathbf{d_{gj}}$ and $\mathbf{d_{dj}}$ are the corresponding path lengths [see Fig. 2(c)], and $A_j^{\alpha\beta}(\theta_{gj},\theta_{dj},\omega)$ is the angular-dependent response or scattering matrix [30] of the target. Apart from the frequency-dependent phase delay in the complex exponent, the only other frequency-dependent term in the model is the target itself; the model implicitly assumes that the response of the measurement system is otherwise broadband. This is justified because the bandwidth of the filter implemented in the imaging algorithm is relatively narrow and in practice dominates the frequency response of the final image (see section 2.1).

The above expression allows the response to any defect to be simulated, subject to the constraint that the generation and detection points must be in the far-field of the defect. Of particular interest are perfect point targets ($A_j^{\alpha\beta}(\theta_{gj},\theta_{dj},\omega)=1$), circular cavities (modeled as scattering matrices computed using the method described in [31]) and straight cracks (scattering matrices computed using the method described in [32]).

2.1. Digital frequency filtering

The bandwidth of the generated ultrasonic signal is determined by the pulse duration of the generation laser, which, in our case, is nominally 1 ns. Due to the laser's short pulse duration, the frequency content of the laser pulse ranges from the low MHz to hundreds of MHz. However, the vibrometer used for detection has a bandwidth limit up to 24 MHz and ultimately sets the limit to the signal captured.

In order to maximize the signal to noise ratio (SNR), the inspection frequency is tuned by means of a frequency-domain digital filter, which is applied to the time-traces during the post processing [33]. First, the raw time-traces ($h_{gd}(t)$) are subject to a Fourier transformation:

$$H_{gd}(\omega) = \int_{-\infty}^{\infty} h_{gd}(t)\exp(-i\omega t)dt \tag{7}$$

where ω is the frequency. Then $H_{gd}(\omega)$ is multiplied with the filter function $G(\omega)$, giving the filtered spectra:

$$S_{gd}(\omega) = H_{gd}(\omega t)G(\omega) \tag{8}$$

$G(\omega)$ was chosen to be a Gaussian filter with center frequency ω_c and 100% bandwidth, at -40 dB. Finally, the positive half of the filtered spectrum only is inverse Fourier transformed to give the analytic (i.e. Hilbert transformed), filtered time-trace that is used in the imaging algorithm:

$$s_{gd}(t) = \int_0^{\infty} S_{gd}(\omega)\exp(i\omega t)d\omega \tag{9}$$

2.2. The total focusing method imaging algorithm

In TFM, the first step is to discretized the target region (in the x, z plane) into a grid. The signals from all elements in the array are then summed to synthesize a focus at every point in the

Optics EXPRESS

grid [25]. The intensity of the image, I(**r**) at any position **r**(x,z) in the scan is given by [25]:

$$I(\mathbf{r}) = \left| \sum_{g=1}^{n} \sum_{d=1}^{n} s_{gd}(t_{gd}(\mathbf{r})) \right| \tag{10}$$

where the double summation is over all combinations of ultrasonic generation (g) and detection (d) positions. The signal $s_{gd}(t)$ is taken from Eq. (9) and the time delay term (t_{gd}) equals:

$$t_{gd} = \frac{d_g(\mathbf{r}) + d_d(\mathbf{r})}{c_T} \tag{11}$$

where $d_g(\mathbf{r})$ and $d_d(\mathbf{r})$ are the distances associated with the generation and detection ray-paths to point **r**.

The response model described previously can be used to simulate the FMC data and resultant TFM image from any configuration of suitable scatterers in order to provide a direct comparison with experimental results. The response model can also be combined with the TFM description to produce what is defined as a sensitivity image, $E(\mathbf{r})$, that describes the amplitude expected from a perfect point target (i.e. one where $A_j^{\alpha\beta}(\theta_{gj}, \theta_{dj}, \omega) = 1$) as a function of position **r**. Let $\theta_g(\mathbf{r})$ and $\theta_d(\mathbf{r})$ denote the angles associated with the generation and detection ray-paths to point **r**. With these conditions, the inverse Fourier transform of the Eq. (6) for the shear-shear mode combination is:

$$h_{gd}^{TT} = \frac{G_T(\theta_g(\mathbf{r}))D_T(\theta_d(\mathbf{r}))}{\left[d_g(\mathbf{r})d_d(\mathbf{r})\right]^{1/2}} \delta\left(t - \frac{d_g(\mathbf{r}) + d_d(\mathbf{r})}{c_T}\right) \tag{12}$$

hence the sensitivity image is:

$$\begin{aligned} E(\mathbf{r}) &= \left| \sum_{g=1}^{n} \sum_{d=1}^{n} \frac{G_T(\theta_g(\mathbf{r}))D_T(\theta_d(\mathbf{r}))}{\left[d_g(\mathbf{r})d_d(\mathbf{r})\right]^{1/2}} \right| \\ &= \left| \sum_{g=1}^{n} \frac{G_T(\theta_g(\mathbf{r}))}{\left[d_g(\mathbf{r})\right]^{1/2}} \sum_{d=1}^{n} \frac{D_T(\theta_d(\mathbf{r}))}{[d_d(\mathbf{r})]^{1/2}} \right| \end{aligned} \tag{13}$$

3. Experimental results

3.1. Samples and experimental setup

Two samples were used in this study, referred to as sample 1 and sample 2. Both samples were made of aluminum blocks with dimensions 90 x 20 x 50 mm. Five reflectors were imaged in each sample, as shown in Fig. 3 and Table 1. All defects were through thickness holes or slots created using wire Electrical Discharge Machining (EDM). The side of the samples, where the laser beams were incident, was polished to a mirror surface, in order to maximize the light reflected to the vibrometer.

The experimental setup is depicted in Fig. 2(a). The generation laser was a Nd:YVO pulsed laser with pulse rise time of 1 ns and 1064 nm wavelength. Its repetition rate was 5 kHz and the average power 680 mW, as measured in front of the sample, corresponding to 136 μJ per pulse. The laser beam was focused by means of a cylindrical lens, to a line of 5 mm length in the y-direction (i.e. perpendicular to the imaging plane) and 0.2 mm width in the x-direction. The incidence angle was 25^o with respect to the normal to the sample surface. This was purely to facilitate the scanning of the generating and detecting laser beams and only has a minor effect on the directivity pattern of the ultrasonic waves. This is because, in metals, the optical penetration

Optics EXPRESS

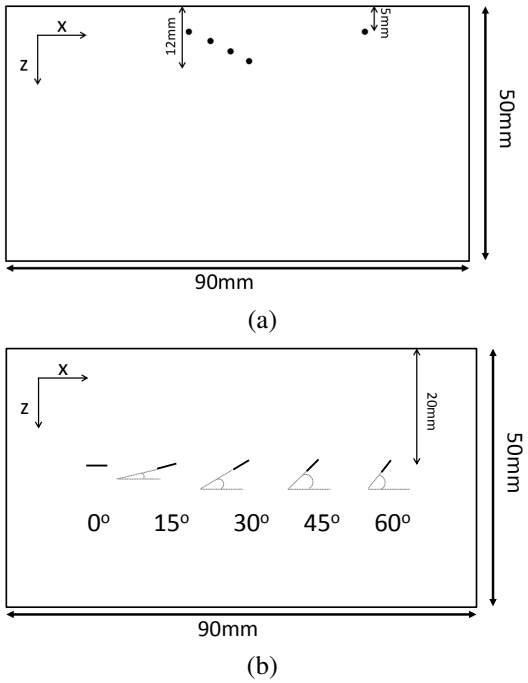

Fig. 3. Schematic diagram of samples 1 (a) and sample 2 (b), side views. Sample 1 has through holes and sample 2 has through slots of orientations ranging from 0^o-60^o.

depth is of the order of nanometers and the laser radiation is absorbed at a very superficial layer, unlike the effect that this angle of incidence would have had in a semi-transparent material, as described in [34]. Aluminum reflects 93% of the incident laser energy and only 7% is absorbed [35]. A Polytech vibrometer (OFV-534 head with OFV-5000 controller) was used to detect the out-of-plane component of the ultrasonic signal. The light of the CW 633 nm HeNe laser that it uses, was focused to a 0.04 mm diameter spot and was aligned with the middle of the generation line source with an angle of incidence 0^o with respect to the surface normal. The power of the detection laser was <1 mW.

Table 1. Details of side drilled holes and slots in test samples.

Sample	Reflector	Depth from surface (mm)	Type	Dimensions (mm)	Orientation (^{o})
1	1	5	hole	Ø1.2	N/A
	2	8	hole	Ø1.2	N/A
	3	10	hole	Ø1.2	N/A
	4	12	hole	Ø1.2	N/A
	5	5	hole	Ø1.2	N/A
2	1	20	slot	3×1	0
	2	20	slot	3×1	15
	3	20	slot	3×1	30
	4	20	slot	3×1	45
	5	20	slot	3×1	60

Optics EXPRESS

During the FMC data acquisition a 1-D LIPA was synthesized. In the case of sample 1, a $n = 89$ element array was synthesized, with element spacing of 155 μm and in the case of sample 2, a $n = 161$ element array was synthesized, with element spacing of 155 μm. The array spacing should be less or equal to half the ultrasonic wavelength to avoid grating lobes and increase the steering angle of the array [36]. The array spacing was chosen here to correspond to half the wavelength of the shear wave at 10 MHz. This guarantees the absence of grating lobes up to 10 MHz; the system can potentially be used above that frequency, but grating lobe artifacts may then be present. To synthesize the LIPA in each case, the sample remained stationary, throughout the experiment, while the detection and the generation laser beams were scanned in turns. The detection laser was scanned across all consecutive array element positions, while the generation laser remained focused at one position. Then the generation laser beam was moved, irradiating another element position and the detection laser was scanned again across all element positions [Fig. 2(b)]. The bandwidth of the vibrometer is from low MHz to 24 MHz, with a flat frequency response across its bandwidth. Each captured waveform was averaged 500 times.

3.2. Results

A 1 MHz high pass, analog filter was applied during the data collection, to reduce some of the signal noise, without loss of useful information. This is because the minimum dimension of the defects for imaging was ~ 1 mm and the ultrasonic wave amplitude from defects falls off rapidly once they are below one wavelength in size (corresponding to shear waves below 3 MHz). These signals tend to contribute mostly noise to the final image which is why the analog filter was used. Digital filtering was applied during the data post processing as described in section 2.1. The digital filters applied had various central frequency values, as specified in each case, with 100% bandwidth, at -40 dB. The shear wave velocity of c_T=3100 m/s was used in Eq. (11). The directivity of the shear wave shows a maximum at 30^o and there was sufficient out-of-plane component to be detected by the vibrometer.

Figures 4(a) and 4(b) show the experimental and the simulated TFM image from sample 1, respectively, using 8 MHz digital filter. The array aperture is also included in the images. Five defects are very well resolved in the experimental image, at depths 5 mm (reflector 1 at x=-17 mm and reflector 5 at x=13 mm from the center of the array), 8 mm (at x=-14 mm from the center of the array), 10 mm (at x=-10 mm from the center of the array) and 12 mm (at x=-6 mm from the center of the array). The agreement between the experimental and simulated results is excellent. The level of intensity of the TFM image (in this and in all subsequent images) in decibel units, is defined as:

$$I_{dB} = 20\log_{10}\frac{I(\mathbf{r})}{I_{max}} \tag{14}$$

where $I(\mathbf{r})$ is defined in Eq. (10) and I_{max} has a single value in each image, corresponding to the maximum intensity of the image at depths>5 mm. This means that images are normalized to the largest defect response, rather than the very high amplitude surface wave artifacts present at shallower depths. The surface acoustic wave (Rayleigh wave) is generated simultaneously with the shear and longitudinal waves. Figure 5 shows a B-scan of received signals at all detector positions, when generation is at the position of the first element and is composed of the same filtered data as those shown in Fig. 4(a). The surface acoustic wave (marked “R” on Fig. 5), is shown as the diagonal line in the scan. The presence of this wave is evident in Figs. 4(a) and 4(c) and it is confined to a region near the surface of the sample. This crosstalk region, where the surface acoustic wave interferes with the results from the shear wave, currently defines a limit as to the minimum depth to which a defect can be detected [37]. The limit is related to the aperture of the array (A), the acoustic velocity of the surface (c_R, taken here as 2900m/s) and the shear (c_T) wave in the material. For example, in the results shown in Fig. 4(a), the array aperture is 13.8 mm, and the crosstalk region will have a duration $t_C = A/c_R$. During this time, the shear

Optics EXPRESS

wave will have traveled a distance equal to $d_T = c_T t_C$. The corresponding minimum depth, for which the signals are unaffected by the surface acoustic wave, given that the experiments are done in pulse - echo mode, is $d_{lim} = d_T/2$. Substituting the corresponding values yields to $d_{lim} = 7.4$ mm. Due to the relatively large number of signals used in the imaging algorithms, the main effect of the surface acoustic wave is restricted to a smaller depth, which, for the results shown in Fig. 4, is of the order of 4 mm, for the TFM images.

Figure 4(d) shows the sensitivity image ($E(\mathbf{r})$), as described by Eq. (13). It can be seen that the sensitivity is not uniform and that there are some "blind spots" where the expected amplitude of response from a point target as a function of position is minimized. As a result, $I(\mathbf{r})$ (shown in Fig. 4(a)) has uniform noise but non-uniform sensitivity. To account for this effect, the normalized image ($N(\mathbf{r}) = I(\mathbf{r})/E(\mathbf{r})$) is shown in Fig. 4(c). $N(\mathbf{r})$ has non-uniform noise (the noise in areas of weak signal is amplified), but uniform sensitivity.

The same data set was used to compose the SAFT images shown in Fig. 4(e). In conventional time-domain SAFT, the waveforms captured from a multitude of transmitter/receiver locations are combined to perform the summation of n signals (the aperture) shifted in time and arriving in phase to a localized region, the focus [38]. The delay law applied in this case, is the same as the one described in Eq. (11), however only the signals corresponding to a fixed transmitter/receiver distance are considered in Eq. (10). In the present paper, the SAFT was implemented after capturing the full matrix, by choosing to include only the measurements where the generation and detection points are coincident; these correspond to the elements on the main diagonal of the full matrix only, marked with a red dotted line in Fig. 2(d) [39]. In Fig. 4(e), the presence of the Raleigh wave is again evident and it is confined to a region ~2mm from the surface. In addition, none of the defects of sample 1 is clearly above the noise level. This is partly due to the random noise being higher than in TFM because each pixel is based on summation of n rather than n^2 signals. If n times more averaging was performed during the SAFT acquisition (so that the total number of laser generation pulses used during data acquisition was the same as for TFM) the absolute noise level in the SAFT image would be the same as in the experimental TFM image. Since the experimental TFM image [Fig. 4(a)] agrees well with the noise-free TFM simulation [Fig. 4(b)], it is expected that experimental SAFT images acquired with n^2 signals would agree with the simulated noise-free SAFT simulation.This is the case shown in Fig. 4(f), which presents the simulated SAFT image. However, comparison of the model images in Figs. 4(b) and 4(f) shows that even in the absence of noise, the SAFT image is poorer than the TFM: it exhibits many imaging artifacts that are of significant amplitude.

Figures 6(a) and 6(b) show the experimental and the simulated TFM images from sample 2, respectively, using 8 MHz digital filter. Five defects can be seen in Fig. 6(a) with high spatial resolution. The agreement between simulated and experimental results is good but not excellent. This is due to the fact that only first order scattering is considered: the model considers the defects as perfectly straight and infinitely narrow cracks, not slots with round ends (which have a higher scattering coefficient than a sharp tip), as in reality. Figure 6(d) shows the sensitivity image ($E(\mathbf{r})$) and once again, it is non-uniform. Figure 6(c) shows the normalized image of the experimental data, where the sensitivity is uniform.

The SAFT algorithm was also applied to this set of data, using the elements of the main diagonal of the full matrix. The results are shown in Fig. 6(e), using 8 MHz digital filter. Overall, the SNR is down by 15 dB between Figs. 6(a) and 6(e) and only one out of five defects (slot of 15^o orientation) is above the noise level in Fig. 6(e). Similarly to the discussion about the SAFT results for sample 1, this is partly due to the fact that n signals are being used for the SAFT image, while the TFM image uses n^2 signals. Figure 6(f), presents the simulated SAFT image using the noise-free model. Once again, comparison of the model images in Figs. 6(b) and 6(f) shows that even in the absence of noise, the SAFT image is poorer than the TFM image.

Figure 7 shows a close up of the TFM results, on the 30^o angle slot of sample 2, using digital

Optics EXPRESS

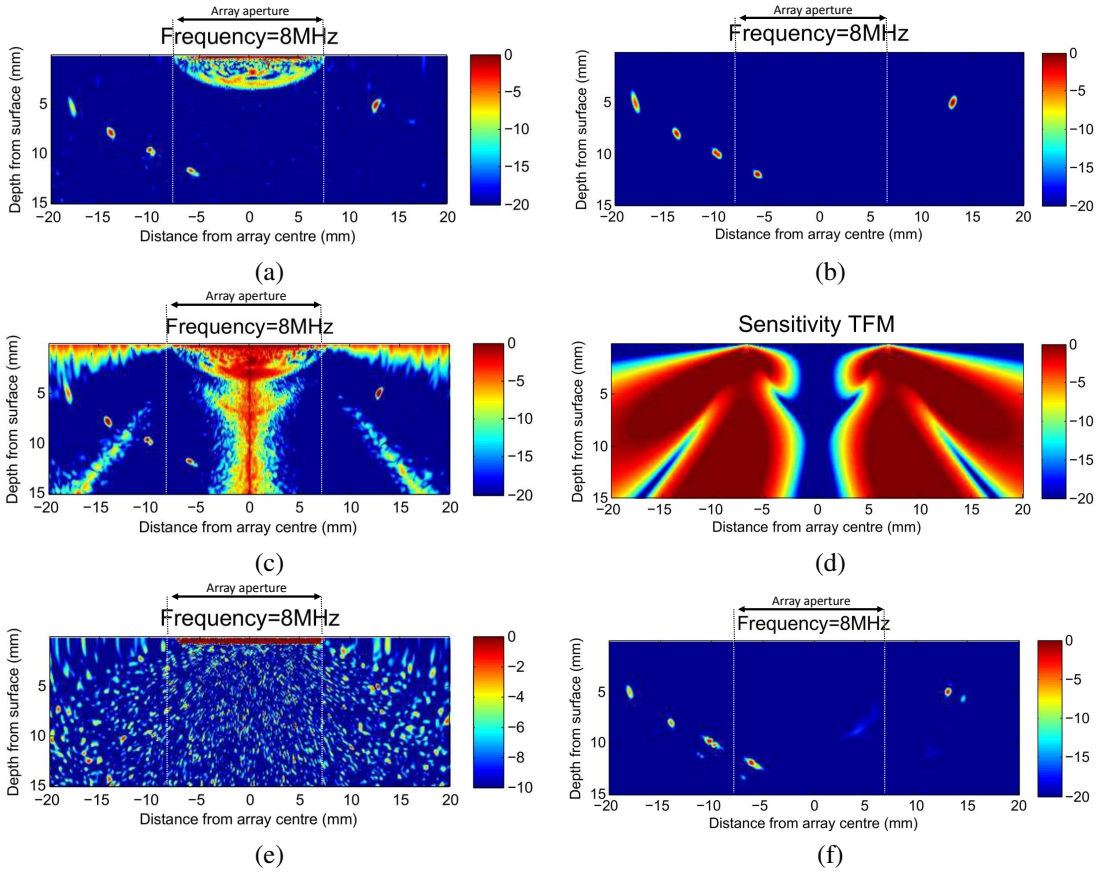

Fig. 4. Images of sample 1: (a) TFM image using experimental data, (b) TFM image using the simulated response model, (c) the normalized TFM image of the experimental data, shown in (a), over the sensitivity, shown in (d), (d) the sensitivity image, (e) SAFT image using experimental data and (f) SAFT image using the simulated response model. The array aperture and the digital filter used in each case are marked on images (a), (b), (c) and (e), as well as the dynamic range used (dB scale).

Optics EXPRESS

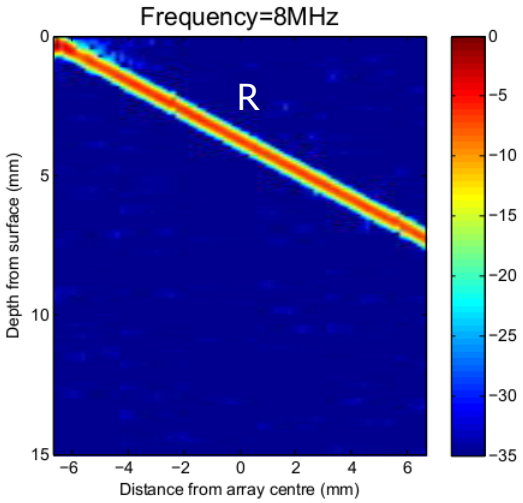

Fig. 5. B-scan of received signals at all detector positions, when generation is at the position of the first element, using the same data as in Fig. 4(a). The surface acoustic wave is marked as "R". The dynamic range is in dB scale.

filters of 4, 7, 10 and 13 MHz central frequency. The defect can be identified in all figures and it is barely above the noise level in Fig. 7(d). The defect is better spatially resolved in Fig. 7(b) and the surrounding image noise drops by at least 7dB between Figs. 7(a) to 7(d).

4. Discussion

Despite the considerable advancement made with the proof of concept of LIPAs presented here, there are still some areas that can be improved. The main issue with the FMC is the need to acquire $n \times n$ signals, making the data acquisition process very time consuming. At the moment, the data acquisition speed is 1.5 points per second, which means in practice that it takes under 5 minutes to capture the full matrix of a 20 element array and 90 minutes for an 89 element array. The speed is currently limited by the mechanical scanning and the data acquisition system and the system is being re-designed to address this issue. The following discussion relates to the fundamental speed limitations of the technique and how to overcome them.

4.1. Optimizing the array spacing

It is possible to perform the post process analysis in a range of frequencies, taking advantage of the broadband ultrasonic signals generated by laser ultrasonics. For the experimental system used in this study, the ultrasonic bandwidth is 1-24 MHz, a limit set by the analog filter and the detection system used. The choice of frequency for the digital filter used can be adjusted to the expected defectsâĂŹ size, the depth and the material properties. Figure 7 shows the post processing of the same set of data: an initial analysis at low frequencies would detect the defects and an analysis at higher frequencies would help to characterize them. Figure 8 shows the extracted intensity level as a function of central frequency of the digital filter used for reflectors no. 4, in samples 1 and 2. In order to compare results between different images, the value of I_{max}, in Eq. (14), was taken as the maximum intensity at a defect location among all the TFM images with different digital filtering. These results are graphically summarized in Visualization 1 and Visualization 2 which present a movie composed of the TFM images for sample 1 and 2 using a series of different digital filters. The Figs. 7, 8 and the visualizations show that all defects

Optics EXPRESS

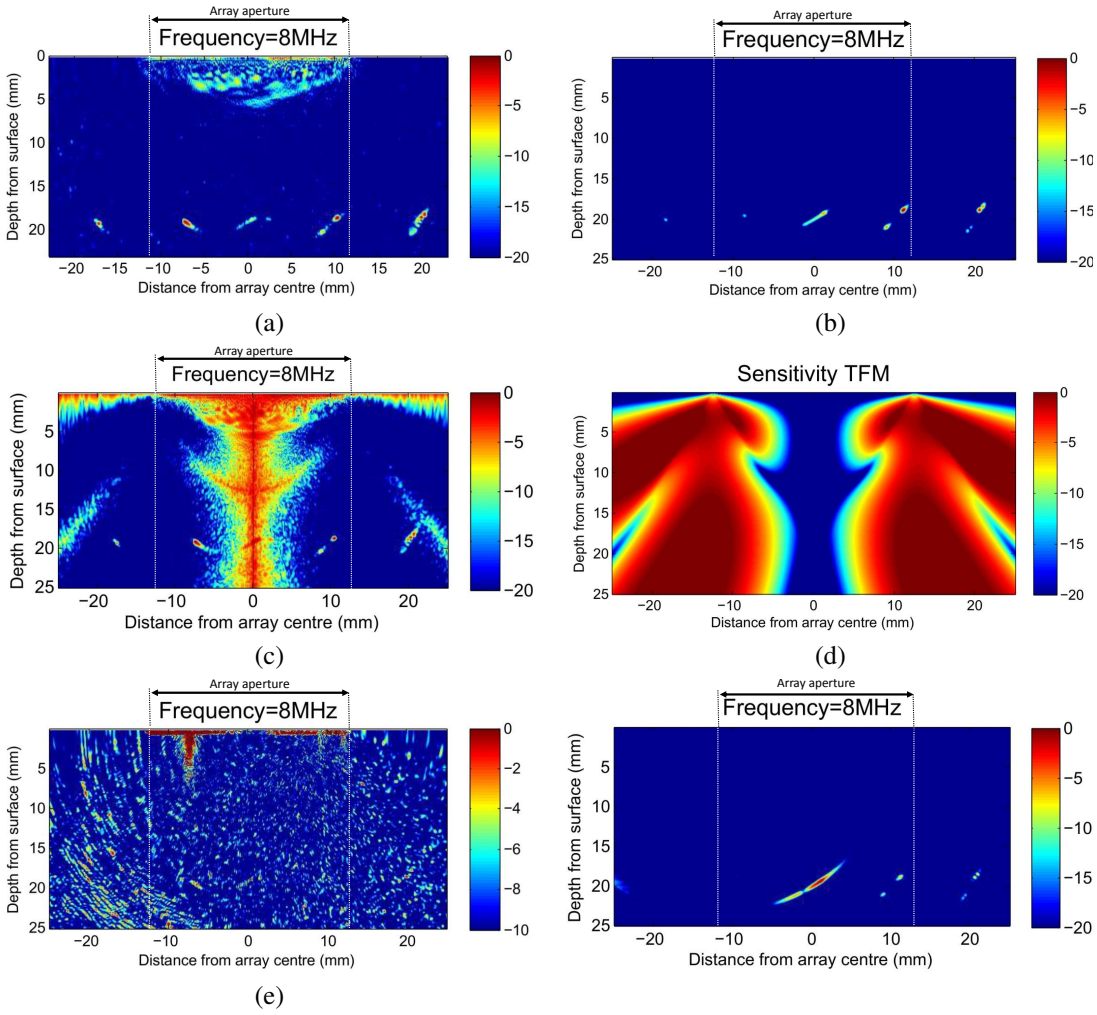

Fig. 6. Images of sample 2: (a) TFM image using experimental data, (b) TFM image using the simulated response model, (c) the normalized TFM image of the experimental data, shown in (a), over the sensitivity, shown in (d), (d) the sensitivity image, (e) SAFT image using experimental data and (f) SAFT image using the simulated response model. The array aperture and the digital filter used in each case are marked on images (a), (b), (c) and (e), as well as the dynamic range used (dB scale).

Optics EXPRESS

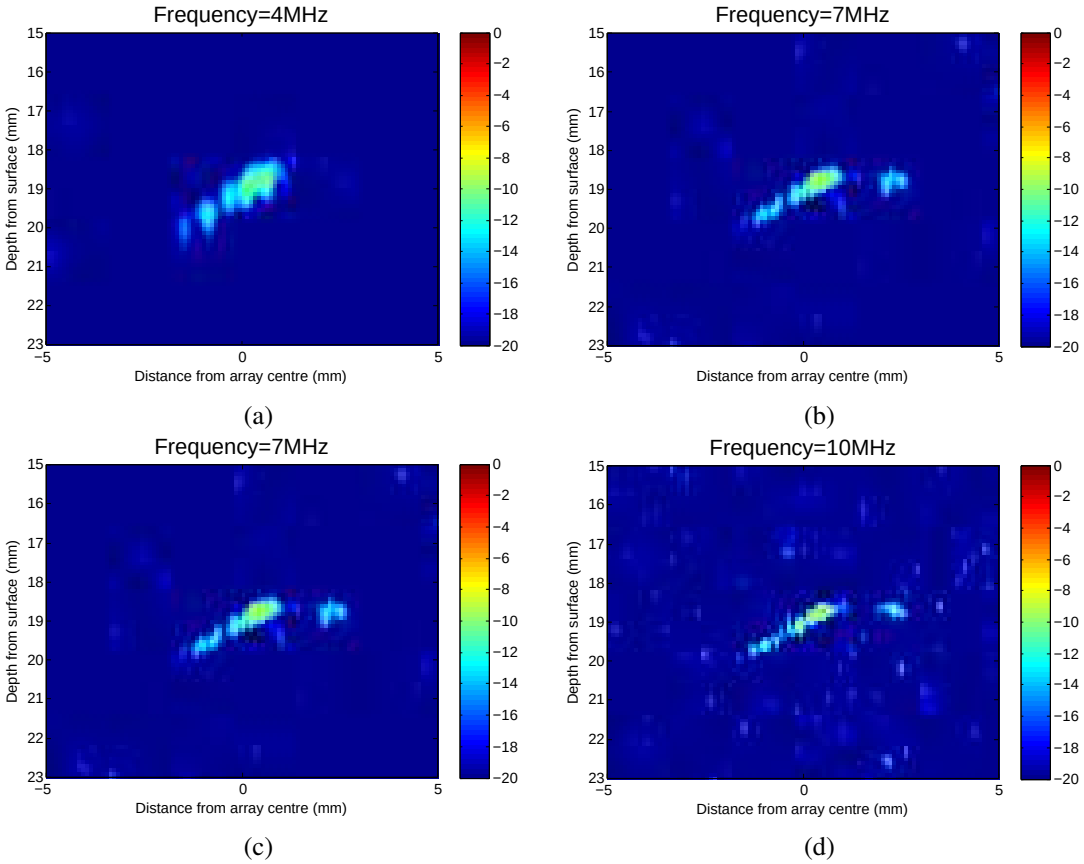

Fig. 7. Detail of the TFM images showing the 30^o angle slot of sample 2 using digital filter of center frequency (a) 4 MHz, (b) 7 MHz, (c) 10 MHz and (d) 13 MHz. The dynamic range of all images is set at 20 dB to facilitate comparison.

are visible when using digital filters between 3-11 MHz and that there is an optimization to reach between overall SNR and lateral resolution. This information can be used to optimize the speed of the data acquisition process, as lower frequencies mean larger array spacing (i.e. fewer array elements for the same size aperture) during data collection. For example, using the information in Fig. 8, a digital filter of 6 MHz would be the most appropriate to image holes located at 12mm depth, hence an appropriate array spacing would be 258 μm, making the data acquisition faster by 1.7 times. However, at the time of setting the experimental parameters, this information was unknown to the authors and the choice of 10 MHz for setting the array parameters proved to be sensible, in order to avoid under-sampling.

In order to visualize the effect of using fewer array elements, Fig. 9(a) shows the TFM image from sample 1, composed from a subset of the full matrix corresponding to an array step of 310 μm and a 44 element array and Fig. 9(b) shows the TFM image using an array step of 155 μm and a 89 element array. Comparison of the two graphs shows a drop in SNR by 6 dB, however, all five defects of sample 1, ranging in depth from 5 to 12mm, can be easily detected. In addition, there is a reduction in volume of data by a factor of 4, resulting in faster processing time and less demanding storage and computational memory capabilities.

Optics EXPRESS

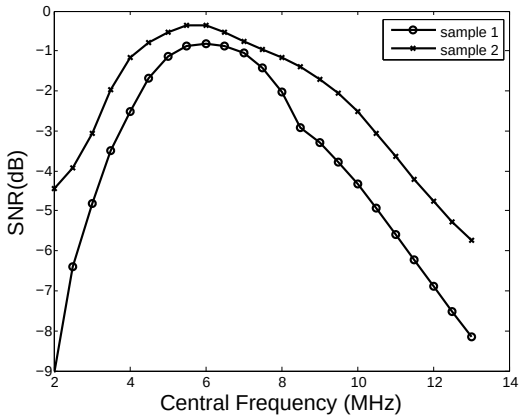

Fig. 8. The SNR of the TFM images, measured at reflectors no. 4 of sample 1 and sample 2, as a function of the digital filter central frequency. Visualization 1 (for sample 1) and Visualization 2 (for sample 2) present the results for all reflectors, as a movie composed of the TFM images using different digital filters.

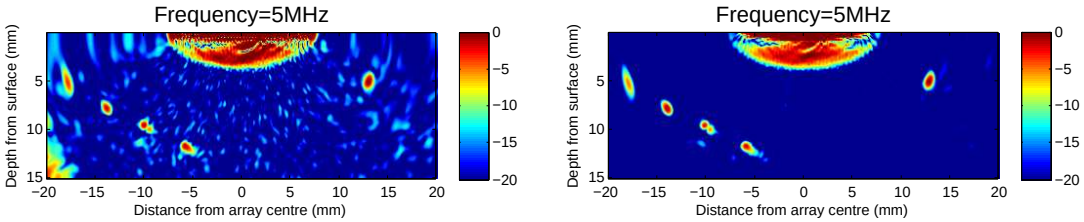

(a) (b)

Fig. 9. TFM image of sample 1 using (a) a subset of the full matrix corresponding to array step of 310μm and 44 element array and (b) the full matrix corresponding to array step of 155μm and 89 element array. A digital filter of 5MHz was applied in post processing and the dynamic range is 20dB in both images.

4.2. *Choosing the repetition rate of the generation laser*

The FMC is time consuming when averaging of multiple signals is needed. This was the case in the work presented, as laser ultrasonic generation at the thermoelastic regime generally produces weak signals. The first improvement proposed here is to chose a laser source with higher repetition rate for the ultrasonic generation. A 5 kHz repetition rate laser was used in this study, however a laser with repetition rate of 10 kHz is just as portable and commercially available and could be used to double the data acquisition rate. It is noted here that there is an ultrasonic limit set by the physical properties of the sample under test: the speed of any ultrasonic imaging process is ultimately limited by the minimum time (t_{min}) required between successive firings to ensure that the reverberations from the previous cycle have sufficiently decayed before the next. In the case of LIPAs, this quantity sets the limit to the maximum repetition rate (F_{max}) of the generation laser that can be used ($F_{max} = 1/t_{min}$). As an example and based on values of attenuation in aluminum published in the literature [40], for an aluminum sample with same physical dimensions as the one in this study, the F_{max} is approx. 15 kHz, corresponding to three times faster data acquisition than the current rate.

Optics EXPRESS

4.3. Lower the number of averages

The theoretical maximum speed of FMC (v_{max}) is determined by the minimum time per FMC frame ($T_{min} = m \times n^2 \times t_{min}$, where m is the number of averages), which is the time taken to acquire one complete full matrix. In the results presented here, each recorded waveform was averaged over 500 signals and a considerable speed improvement is expected by lowering this number, which can be achieved by increasing the SNR of the recorded signal. For a laser ultrasonics system using an interferometer, the SNR, measured as the quotient given by dividing the root-mean-squared signal current by the root-mean-squared noise current, is related to the surface displacement (δ), the optical power reaching the detector (P_D) and the bandwidth (B_D) of the detection system, via the following proportionality [41]:

$$SNR \propto \delta \sqrt{\frac{P_D}{B_D}} \tag{15}$$

In the thermoelastic regime, the amplitude of the displacement of the bulk waves increases linearly with increasing the generation laser power, P_G [42], i.e. $\delta \propto P_G$. At a first glance, increasing the SNR could be achieved by increasing P_G. However, for the experiments presented, the laser power is already set at the limit before damage occurs (damage threshold in aluminum is ~150 kW/mm^2 [21]). Another option is to increase the reflected light power, P_D. Given a certain surface finish of the tested sample, increasing the power of the detection laser will improve the SNR [43]. Care should be taken to remain at the nondestructive regime, as a high power detection laser could damage the sample. The vibrometer used in this study is of very low laser power (<1mW) and a higher power laser would be more appropriate. Long pulsed lasers (of the order of 10's of microseconds) have been successfully used by other authors. For example, in [44] a laser of 50 μs pulse duration and high peak power of 1.5 kW was used as part of a Confocal Fabry-Pérot interferometer, testing black carbon fiber composite panels, using laser ultrasonics, without surface treatment. In our study, the surface of the sample was polished to a mirror finish, to increase the amount of light reflected to the vibrometer. An interferometer of different design, developed for rough surfaces, such as the Confocal Fabry-Pérot [45] or one based on the photorefractive effect [46,47] could be used to avoid surface modification.

In order to give a realistic example of what the effect of some of the suggested improvements would be to the system, assuming a detection laser of 100 mW power, and full light return from the sample, an increase of SNR by a factor of 10 compared to the existing setup, would be observed. This would lower the number of averages by a factor of 10^2 and averaging of only a few pulses would be required. If no averaging were required, the theoretical limit for the FMC, would be $n^2 \times t_{min}$, limited only by the repetition rate of the generation laser. If a laser with repetition rate of 15 kHz were to be used, for a phased array of 89 elements, this would correspond to 500 ms for the entire full matrix. There is also a processing time needed to convert the FMC data into an image, but this is limited only by computational speed. In practice there are a number of additional factors in the data acquisition system that reduce the overall scanning rate, primarily due to the mechanical scanning system and the oscilloscope used to acquire data. For our existing experimental setup, these factors increase the time per FMC frame by around 7 times, compared to the theoretical limit and currently, the data collection system is being re-designed. One possibility is to use single generation, multiple detection version for the FMC, which would eliminate or minimize scanning of the detection system. This could be achieved by using optical phased array detection, such as the multiplexed two-wave mixing optical array interferometer presented in [48].

Another option that would reduce the number of averages, is to modulate the spatial intensity distribution of the generation laser beam, using Hadamard multiplexing, which has been shown to improve the SNR [37]. In [37], an improvement of SNR by $F = 2.8$ was observed. This is equivalent to the SNR improvement obtained by increasing the number of averages by a factor

Optics EXPRESS

of $2.8^2 = 8$. Put the other way round, this implies that such Hadamard multiplexing enables the number of averages to be reduced by a factor of 8 without affecting the final SNR. In the present study, a similar improvement to the system, would reduce the number of averages from 500 to 60, increasing the data acquisition speed by a factor of 8 as well.

5. Conclusions

The results presented here give the first experimental demonstration of the benefits of using the FMC data acquisition method and the TFM as a post processing algorithm in laser ultrasonics. The beamforming and steering of the ultrasound is done during the post processing, resulting in a laser induced phased array with significantly improved spatial resolution and defect detectability. Results have been presented from aluminum samples with defects ranging at depths from 5 mm to 20 mm and of various orientations. Comparison of the experimental results with simulations based on the model presented, shows very good agreement.

The technique is non-contact and nondestructive and would be attractive for applications such as inspection of carbon fiber composites or welded parts in microelectronics, performing NDT in hazardous environments or at the production line. LIPAs could be applied in optically based acoustic microscopy, where the high frequency component of laser ultrasonics can outperform the conventional transducers, providing thickness measurements or the profile of the interface between multi-layered thin films. Another application could be an optical based version of the ultrasonic speckle image correlation [49], for mapping mechanical properties of the material.

The system can be easily fiber coupled to address places of limited access, and can accommodate complex geometries. The lasers themselves are relatively small and portable. Using optics makes the array elements easy to manipulate: change spot size and scan. The FMC allows post processing in a range of different algorithms. In this study, the same data set has been used to compose a TFM image and a SAFT image. Both these algorithms allow the detection of defects outside the array aperture. Comparison of the results between the two imaging algorithms has shown that the TFM improves the spatial resolution. Although the SAFT algorithm using n^2 signals will probably exhibit similar detectability to the TFM, the image quality and hence ability for defect sizing and characterization will be worse. In addition, capturing n^2 signals for the SAFT algorithm would require as much time for data collection as acquiring the full matrix. In this case, the FMC has the advantage of being able to be used with a range of imaging algorithms, including the TFM, which can only be performed when the full matrix is known.

Laser ultrasonics is a broadband technique and this allows the results to be post processed in a range of frequencies, a significant advantage over the conventional transducers. The choice of frequency can be adjusted according to the expected defect size, depth and material properties and this will have an effect on the optimization of the process both in terms of the desired resolution and on the speed of the process (data acquisition and computation time).

The main concern regarding FMC coupled with laser ultrasonics is the time for data acquisition. Improvements are proposed in this paper that address making data acquisition faster. This discussion has assumed that the computational speed for the TFM is faster than the data acquisition speed. Recent improvements in data transfer protocols and GPU-based processing have dramatically increased the speed for acquiring the TFM image. Based on these hardware developments, it is expected that the theoretical speed limit for LIPAs using FMC will be approached within the next few years.